1993

Geometry of isothermal and isoconcentration surfaces in thermal turbulence

B. J. Gluckman

H. Willaime

Jerry P. Gollub
Haverford College

Repository Citation

"Geometry of Isothermal and Isoconcentration Surfaces in Thermal Turbulence," B.J. Gluckman, H. Willaime, and J.P. Gollub, Phys. Fluids A 5, 647 (1993).

Geometry of isothermal and isoconcentration surfaces in thermal turbulence

B. J. Gluckman, H. Willaime, and J. P. Gollub

Additional information on Phys. Fluids A

Geometry of isothermal and isoconcentration surfaces in thermal turbulence

B. J. Gluckman, H. Willaime,[a] and J. P. Gollub
Department of Physics, Haverford College, Haverford, Pennsylvania 19041 and Department of Physics, University of Pennsylvania, Philadelphia, Pennsylvania 19104

The geometry of isothermal surfaces for Rayleigh–Bénard convection at Rayleigh numbers R in the range 10^7 to 3×10^8 (close to the soft to hard turbulence transition) are measured. The measurements were made by imaging the color of light scattered from chiral nematic particles suspended in the fluid. Although the isotherms are multiply connected and convoluted, they do not display fractal scaling. The minimum scale for convolutions can be understood as resulting from the competition between folding and thermal diffusion. The isotherms are characterized statistically by the probability distribution of the local curvature, which may be described approximately as a stretched exponential. The distribution is essentially independent of the position and orientation of the plane of observation, and of R over the range explored. The geometry of the isotherms is compared to that of isoconcentration surfaces for dye injected into the flow; the latter do show a limited range of approximate fractal scaling because of the smaller diffusivity of the dye. The thermal measurements are supplemented by simultaneous measurements of the velocity field obtained by particle image velocimetry. Unstable waves often form on the thermal boundary layers in regions of high horizontal velocity gradient.

I. INTRODUCTION AND BACKGROUND

Thermal turbulence generated by a vertical temperature gradient in a closed volume of fluid is a well-controlled phenomenon that challenges our ability to understand the progressive development of disorder resulting from instabilities.[1] Advances in measuring instrumentation that allowed precise local measurements of velocity and temperature fluctuations, along with qualitative visualization of the thermal boundary layers and plumes, have led to considerable progress in understanding thermal turbulence. The object of the present investigation is to extend these earlier studies by quantitative measurements of the temperature *field*, especially the geometry and statistical properties of the isothermal surfaces. This is achieved by digital analysis of the light scattered by small particles of chiral nematic liquid crystal that are suspended in the flow. Their hue provides a sensitive measure of the local temperature, and image processing allows spatial information to be obtained in real time. The geometry of the temperature field is then compared with that of the concentration field of a neutrally buoyant impurity that is mixed by the flow after local injection.

It has long been evident that the temperature field and its isothermal surfaces must be fairly complex when the flow is turbulent. In this study, we characterize this complexity more precisely, and address questions such as the following: What determines the minimum length scale for convolutions of the isotherms? How can these convolutions be characterized statistically? Are these properties substantially anisotropic? Is there a large difference between the

spatial structure of isotherms and that of isoconcentration surfaces for dispersal of a molecular impurity? In order to place this work in context, and to explain the significance of these measurements of the temperature field, we begin by reviewing previous experimental and theoretical studies that bear on the problem of the *geometrical structure of the temperature field* in thermal turbulence.

A. Boundary-layer dynamics

The basic structure of thermal turbulence in a closed cell consists of thin boundary layers that emit plumes at irregular intervals into the interior of the flow. This structure was revealed, for example, by Sparrow *et al.*[2] using an electrochemical technique to change the color of fluid near the isothermal boundary. Tanaka and Miyata,[3] using the same technique at higher Rayleigh number (R), observed that plumes occur in the form of sheets. Later, Asaeda and Watanabe[4] used alumina flakes to visualize the structure of the velocity field near the boundary layer. They noted polygonal patterns of lines toward which the fluid converges in the plane before moving upward. These lines were postulated to be the nucleation sites for plume eruption.

The thermal boundary layers are not quiescent. Propagating undulations in the "thickness" of the thermal boundary layer have been observed using optical interference techniques.[5] Zocchi *et al.*[6] used encapsulated liquid crystal particles which change color with temperature to visualize the thermal field, and described the life cycle of large events at fairly high R (10^9). Erupting warm plumes break off from the lower boundary layer and traverse the cell to the upper boundary layer where they excite waves. The waves can lead to the formation of cold plumes which then descend to the lower boundary layer, where they again stimulate waves. These authors also describe "spiral-

[a] Permanent address: Laboratoire de Physique Statistique, Ecole Normale Supérieure, 24 Rue Lhomond, 75231 Cedex, France.

ing swirls," which are basically regions of the thermal boundary layer that have been folded into a spiral. Using pairs of point temperature probes near the edge of the thermal boundary layer, they measured a velocity–wavelength dispersion relationship for these excitations.

Some of the qualitative features of the thermal boundary-layer dynamics have been studied in recent theoretical and computational work by Shelley and Vinson.[7] They considered a simple two-dimensional model of shear across a density step function (representing the stratification of the unstable boundary layer). They noted a continuum of structures, some of which resemble the plumes and swirls noted experimentally.

B. Transitions in thermal turbulence

In a series of investigations based on heat flux and point temperature measurements in low-temperature helium gas, Heslot et al.,[8] Sano et al.,[9] and Wu and Libchaber[10] identified a number of turbulent regimes as a function of R. They referred to the behavior in the range $5 \times 10^5 < R < {\sim}4 \times 10^7$ as "soft" turbulence; its development is characterized by a loss of coherence between temperature fluctuations at two probes in different locations. Above $R = 4 \times 10^7$, a regime of "hard" turbulence is associated with an exponential probability distribution function (pdf) for the temperature at the center of the cell, scaling of the heat flux as a power law R^β with $\beta = 2/7$, and emergence of a large scale flow.[11] Additional transitions were identified by changes in the power spectra of the local temperature at $R \approx 10^{11}$ and 10^{13}.

Solomon and Gollub,[12] using the liquid crystal imaging method described in the present paper to visualize the thermal field, noted a significant qualitative difference between the "soft" and "hard" turbulence regimes. In the former case, the plumes are coherent across the full height of the cell, whereas in the latter case, they are broken up before traversing the cell. They also found that the shapes of the temperature pdf's for soft turbulence are strongly dependent on aspect ratio. Both the aspect ratio dependence of the pdf's and the coherence of plumes for soft turbulence were subsequently noted in three-dimensional numerical simulations by Christie and Domaradzki.[13] Experimental results of Wu and Libchaber[10] show that *in the hard turbulence regime* both the non-Gaussian form of the pdf's and the 2/7 power law for the heat flux are independent of aspect ratio.

A complete theoretical understanding of these transitions is not yet in hand. However, Castaing et al.[14] found that they could explain the scaling laws observed for the heat flux, the temperature fluctuations in the center of the cell, and the velocity fluctuations, by introducing a mixing layer into the classical model of two marginally stable boundary layers separated by a fully turbulent interior. This phenomenological model does not account for the transitions observed in the power spectra at $R = 10^{11}$ and above. Shraiman and Siggia[15] showed theoretically that the 2/7 scaling law for the heat flux follows from the assumption that the large-scale flow creates a turbulent viscous boundary layer that shears the thermal boundary layer,

causing additional heat to be removed from it. This approach is generally consistent with experiments by Solomon and Gollub,[16] who measured the extraction of heat from the boundary layers by artificial flows comparable to the natural large-scale flows

C. Fractals in mixing

In an alternate theoretical approach, Procaccia et al.[17] considered the geometry of the thermal field. They proposed that isoscalar surfaces in turbulent flows are wrinkled and possibly fractal above a length scale λ^*. This scale is determined by a balance between the diffusivity, which tends to smooth out the scalar field, and the stretching and folding of isoscalar surfaces by the turbulence. They suggested that transitions in local temperature measurements are observed as this length scale passes through the other length scales of the system: the full height of the cell, the size of the mixing zone, and the thickness of the boundary layer.

These investigators predicted an upper bound to the fractal dimension of such a wrinkled isoscalar surface, and an estimate of the length scale λ^* above which one might observe fractal scaling. To do this, they considered the stretching of a Lagrangian volume of fluid containing the isoscalar surface, and used geometric measure theory to estimate its area. The resulting estimate for the area δA_r of the isoscalar contained within a sphere of radius r is as follows:

$$\frac{(\delta A_r)^2}{0.5 r^4} \leqslant c_3 + \frac{c_2}{\kappa} r \delta u_r + c_1 O(r^2), \tag{1}$$

where the constants c_n are derived from the Boussinesq equations, κ is the scalar diffusivity (as appropriate for heat or material diffusion), and $\delta u_r = |u(x) - u(x+r)|$ is the size of the typical velocity fluctuations at scale r. The lower length scale λ^* is taken to be the crossover point of the relative sizes of the first and second terms on the right-hand side of this equation. For small r, the constant term c_3 dominates, and the variation of areas with r is appropriate for a smooth surface. For larger r, the second term dominates, and the scaling of δu_r with r then affects the scaling of areas. If velocity fluctuations are assumed to vary as $\delta u_r \sim |u_0| (r/d)^\zeta$ (where u_0 is the integral velocity scale), this argument leads to the conclusion that isoscalar surfaces should be fractal with dimension $D = 2.5 + \zeta/2$. For Kolmogorov scaling, $\zeta = 1/3$, so D is predicted to be 2.67. [However, for the outer boundary of a turbulent region, they proposed that $\delta u_r \sim |u_0| (r/d)^{\zeta + D - 3}$, so that in this case $D = 2 + \zeta = 2.33$ instead.[18]] The lower cutoff scale was estimated to be

$$\lambda^* = \eta \left(c \frac{\kappa}{\nu} \right)^{1/(1+\zeta)}, \tag{2}$$

where η is the Kolmogorov scale and $c = c_3/c_2$ is a constant independent of Reynolds number. It is of course quite uncertain whether these results apply to turbulent convection at the modest Rayleigh numbers we are able to reach.

648   Phys. Fluids A, Vol. 5, No. 3, March 1993

Gluckman, Willaime, and Gollub   648

The scaling of spatial power spectra of passive scalar contaminants has been known since the work of Obukhov and Corrsin, who independently showed that the power spectrum of temperature fluctuations at wave vector k of $E_\theta(k) \propto k^{-n}$, where $n = 5/3$. This scaling applies for turbulent flows within an *inertial–convective subrange*, bounded at large k by the the limit that both $k\eta < 1$ and $k\eta_\theta < 1$, where $\eta_\theta/\eta = (\mathrm{Pr})^{-1/2}$.[19] Kraichnan[20] has commented that the scaling of the power spectrum of a passive scalar field leads to a fractal description of isoscalar surfaces with fractal dimension $D = (7 - n)/2$, and that in the inertial–convective subrange, $n = 2 - \zeta$.

The observation that isoscalar surfaces appear wrinkled in complex flows with a wide range of length scales has prompted researchers to test these surfaces for fractal scaling. For example, Prasad and Sreenivasan[21] measured the dimension of dye isoconcentration surfaces using laser-induced fluorescence. For both a turbulent axisymmetric jet and planar wake flows, they obtained an average fractal dimension of 2.36 in the scaling range between the integral and Kolmogorov length scales, consistent with the proposed scaling for an interface at a turbulent–laminar boundary. In later work,[18] they noted that a higher value consistent with 2.67 is obtained if the scalar interface is taken to be within the fully turbulent region of the flow, instead of at its edge. In other experiments, Miller and Dimotakis[22] did *not* find well-defined fractal behavior for turbulent jets using time series measurements at a point, and along a line perpendicular to the flow direction. In response, Sreenivasan and Juneja[23] have argued that, at least for relatively low Reynolds number flows, temporal data interpreted as spatial data by means of Taylor's hypothesis do not tend to scale as well as their purely spatial counterpart.

Isoscalar surfaces have also been studied for nonturbulent flows. For example, Ramshankar and Gollub[24,25] studied mixing by modulated surface waves. They found that isoconcentration lines in a plane evolve toward complex curves with a dimension close to 1.4 over a reasonable scaling range. Procaccia and Constantin[26] have predicted an upper bound of 3/2 for this experiment using techniques similar to those in Ref. 17. Ramshankar and Gollub also found that the square of the gradient of the concentration field could be adequately described as a multifractal. This behavior seemed consistent with simple dynamical models studied by Ott and Antonsen,[27,28] who showed numerically that under rather general assumptions, a two-dimensional chaotic flow often concentrates material gradients onto a multifractal.

II. METHODS

A. Convection cell

The convecting fluid is a layer of water, bounded by two horizontal isothermal surfaces. The lower one is a copper block that is resistively heated and regulated electronically. The upper surface is a sapphire window, maintained at constant temperature by a continuous flow of water from a constant temperature bath. The side walls, available in several different heights, are made of 5/8 in. Plexiglas. The inner horizontal dimensions of the convection cell are 6.3×6.3 cm, and the depth d is either 5 or 9 cm. The cell is enclosed in a larger Plexiglas box, maintained close to the mean working temperature of 25.6 °C in order to minimize thermal leakage through the side walls. The ranges of accessible Rayleigh numbers for the 5 and 9 cm cells are 7×10^6 to 3×10^7, and 4×10^7 to 3×10^8, respectively. At the upper ends of these ranges, the overall vertical temperature difference is about 30 °C, considerably beyond the range of validity of the Boussinesq approximation of position-independent fluid properties. Boundary temperatures are measured using thermistors embedded in the copper block and inserted in the entrance and exit lines of the cooling flow near the sapphire window. Fluctuations in R are typically well below $\pm 0.5\%$.

B. Color imaging method

To study the geometrical structure of the temperature field, we seed the flow with small particles which change color with temperature. The particles are composed of chiral nematic liquid crystal, encapsulated in gelatin spheres. They act as Bragg scatterers of visible light, and the most strongly scattered wavelength is highly temperature dependent. The particles are manufactured for use in coatings to visualize temperatures on surfaces. A review of the use of liquid crystals in flow visualization and thermometry can be found in Ref. 29, as well as in a recent experimental paper by Dabiri and Gharib.[30] The particles used here have a mean diameter of 15 μm, small enough that the settling speed ($\sim 4 \times 10^{-4}$ cm/sec) is much smaller than the typical flow speed. The fractional concentration is relatively low, approximately 4.5×10^{-4}. The viscosity of the fluid is not significantly affected by the particles.

We illuminate the cell using white light from a xenon arc lamp. After filtering out the UV light, which is harmful to the particles, we concentrate the light into a thin sheet typically 1.7 mm thick (full width at half-maximum) within the convection cell. The thickness, position, and orientation of the light sheet are adjustable. A color video camera (Panasonic F250) oriented perpendicular to the light sheet is used for data acquisition. The camera has three separate charge-coupled device arrays, for the red, green, and blue (RGB) color bands, to obtain better color resolution than a single-chip camera would provide. A super VHS signal from the camera is recorded on videotape.

During playback and processing, the signal from the videotape is decoded into RGB signals and digitized using a color image processor (Data Translation DT-2871 and DT-2858). The image processor can digitize the signal directly into hue–saturation–intensity (HSI) color space. In this color system, *hue* is a measure of the peak wavelength in the signal, *saturation* is a measure of the color contrast, and *intensity* is a measure of the total light intensity. HSI space is more convenient than the common red–green–blue (RGB) color space since the local temperature is a function of the wavelength of the scattered light, which in turn is closely related to the hue.[31] The spatial resolution in each of the three HSI buffers is 512×480 pixels, and each
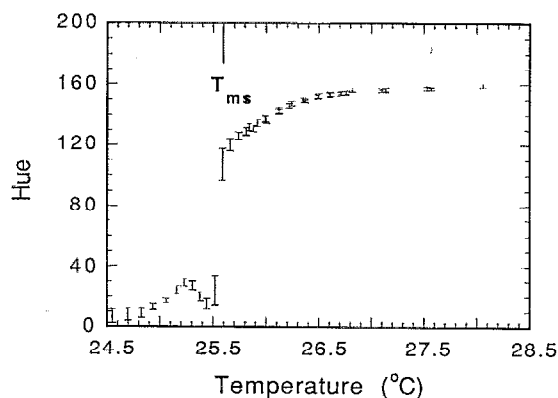
FIG. 1. Measured hue of light scattered at 90° by the chiral nematic particles, as a function of temperature. The steep decline near the "most sensitive" temperature $T_{ms}=25.6$ °C leads to high sensitivity for detecting a particular isothermal surface.

of these quantities has 256 levels. The particle density is on the order of 3×10^5 cm^{-3}, or 20 illuminated particles per pixel on the image plane. Not all of the particles are properly oriented to scatter light at a given instant. As a result, the root mean square (rms) pixel-to-pixel intensity variations are $\pm10\%$.

At temperatures below approximately 25 °C, the liquid crystal is in a smectic phase, and the particles scatter little light. As temperature is increased, a transition occurs to the chiral nematic phase, where the rodlike molecules are aligned within parallel planes, but the local orientation field is slightly rotated between planes. The peak scattering wavelength is determined by the pitch of the resulting helix. Just beyond the phase transition the pitch is small, so only long wavelength light is scattered. As the temperature is increased, the pitch angle increases; this reduces the dominant wavelength of the scattered light. As a result, colder regions of the flow appear red, and warmer regions appear blue.

We calibrate the response of the particles and the measurement system by first setting the cell to a constant temperature and stirring it with a magnetic stirring bar. We then measure the temperature with an internal probe, and spatially average the hue field. This process is repeated at intervals of 0.05 °C through the response range of the particles. The resulting calibration (hue versus temperature) is shown in Fig. 1. The error bars reflect the rms fluctuations of the hue field at constant temperature. Low hue values correspond to the red part of the spectrum, and high values correspond to blue, with green between them. The curve though highly nonlinear, is monotonic over most of its range. We use the steep decline at the "most sensitive temperature" $T_{ms}\equiv25.6$ °C to measure the spatial structure of a particular isotherm with high sensitivity. The boundary temperatures of the convection cell are varied with respect to T_{ms} to explore the structures corresponding to either the mean cell temperature or the temperature at the edge of the thermal boundary layer.

The temperature of greatest sensitivity is a few tenths of a degree above the smectic-to-nematic phase transition.

When we study the isotherm near the mean temperature of the system, some of the fluid is far below this transition, and hence appears dark. This is useful for imaging of boundary-layer events, where there are large thermal gradients and a known condition at the wall. For example, with T_{ms} set between the cold boundary temperature and the mean cell temperature, the upper thermal boundary layer appears as a dark region attached to the wall and bounded by a brighter region. However, cool plumes in the interior have low color contrast and are harder to interpret. For this reason, we frequently use information from the intensity and saturation fields to avoid ambiguous hue values from regions cooler than 25.2 °C.

An example of the scattered light field from a vertical plane is shown in color in Fig. 2(a). Here T_{ms} is equal to the mean cell temperature, halfway between the two boundary temperatures. Plumes can be seen emerging from the upper and lower boundary layers, but the color changes in the interior are relatively weak. The color contrast may be increased by looking only at the hue variable, as shown in Fig. 2(b). The isotherm corresponding to T_{ms} is at the boundary of the blue region. The hue field has considerable small-scale noise due both to variations in the light scattered from individual particles, and to noise inherent in the color video signal.

C. Finding isotherms

In order to reduce the measurement noise, we smooth the image using a combination of spatial decimation and convolution. The spatial decimation involves mapping an area 2 pixels by 2.5 pixels onto a single pixel (compressing the number of points by 2 in the x direction and 2.5 in the y direction). This process both smoothes the data, and adjusts the lattice so that squares in the image correspond to squares in real space. The subsequent smoothing convolution kernel is a 5×5 array with a mean radius of about 1.6 pixels. To summarize, the combination of decimation and convolution smoothes the image by a factor of approximately 3 overall.

Isotherms are then identified by first searching for unidentified crossings of the hue variable through the selected threshold, and then following the resulting isotherm clockwise around the region of the image where the hue is below the threshold hue (or temperature) value, while saving the isotherm coordinates. This process is repeated until all crossings in the area of interest have been found. It is only necessary to store the isotherms to a precision of 1 pixel in the smoothed and decimated field, because the pixel size is less than the half-width of the smoothing peak and the thickness of the light sheet. Figure 2(c) shows the final smoothed hue field, with the isotherm corresponding to the mean temperature outlined in white. (The narrow thermal boundary layers themselves are obscured due to reflections and parallax.) The pixel size in this final photograph, as in all the isotherm data presented here, is 0.37 mm; this may be compared to the 5 cm height of the cell. Our smoothing algorithms reduce the resolution to ~0.6 mm, and the thickness of the light sheet leads to a final effective resolution of approximately 1 mm.
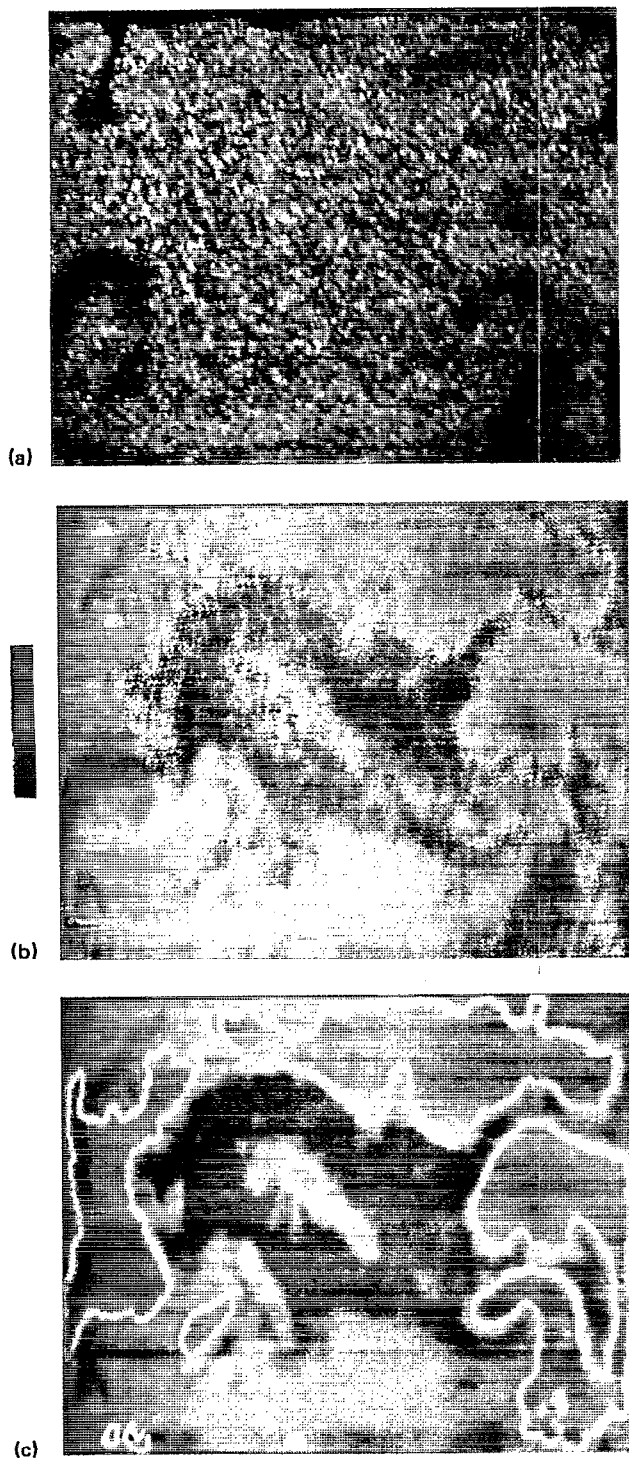
(a)

(b)

(c)

FIG. 2. Color images of light scattered from a vertical light sheet, at $R = 3.4 \times 10^7$. (a) Unprocessed image. (b) Hue field corresponding to (a), with the saturation and intensity set equal to constants. The color bar is linear in temperature over the range $T_{ms} \pm 2$ °C; regions warmer than the mean cell temperature are blue. (c) Smoothed hue field, with the isotherm at the *mean* temperature outlined in white.
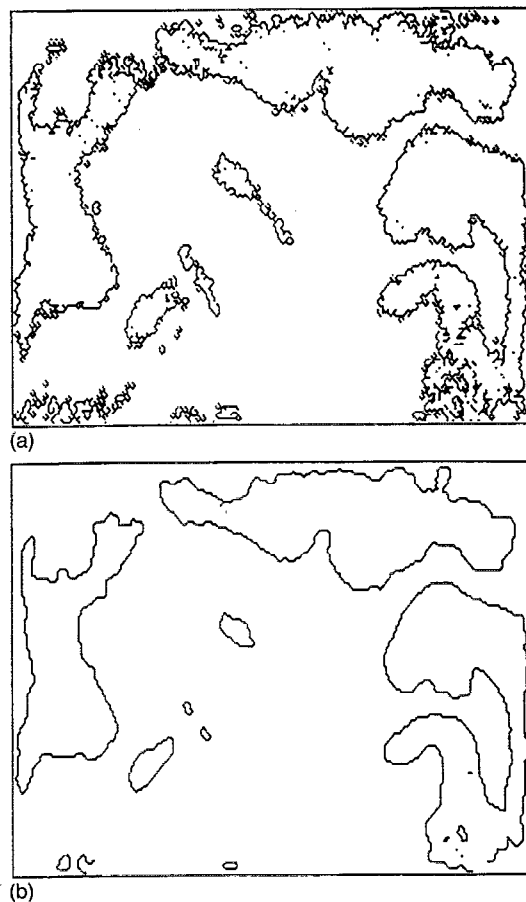

(a)

(b)

FIG. 3. Mean isotherm derived from the hue field of Fig. 2, with different amounts of noise reduction. (a) After decimation (compression by a factor 2.0 along x and 2.5 along y). (b) With an additional smoothing convolution as described in the text.

In order to display the degree of noise reduction due to the smoothing algorithm, we plot in Fig. 3 the isotherm of Fig. 2(c) before and after smoothing. The small-scale structure in (a) is smaller than the thickness of the light sheet (roughly five pixels in that panel), and should therefore be considered to result from measurement noise. The structure on larger scales is essentially the same before and after smoothing, and hence may be regarded as representing the actual structure of the isotherm. It is impossible to be certain that there are no significant "unresolved" features in the isotherm shapes, but our belief is that the isotherms are fully resolved by the measurement methods described here.

D. Measuring the velocity field

We also determine the velocity field from the same video images using a technique based on particle image velocimetry (PIV). A discussion of multipoint velocity measurement techniques, including PIV, can be found in Ref. 32; its adaptation for use with video images has been demonstrated by Willert and Gharib.[33] The technique utilizes the fact that the intensity fluctuations in the images correspond to light scattered by individual particles that move coherently. The method assumes that within a short time interval, particles within a small interrogation area will merely be advected a small distance by the flow. This displacement can be extracted by computing the cross-correlation function between corresponding areas (typi-

cally 24–32 pixels or 3–4 mm in size) in two images. The position of the main peak in the cross-correlation function is proportional to the local velocity, averaged over the selected interrogation area. Optimization of this technique involves balancing the size of the interrogation area, the time difference between the images that are compared, and the particle density. The method deteriorates, for example, when the mean displacement is too large or when the flow is strongly three dimensional so that particles are advected quickly out of the plane of illumination. Our time resolution is typically 0.13 sec.

E. Dye transport

In order to study the mixing of a passive impurity with lower diffusivity, we inject a water soluble fluorescent dye solution (uranine) through a port in the center of the lower isothermal boundary. The radius of the injection nozzle is about 0.05 cm, and the Reynolds number of the injection is close to unity. A horizontal section of the cell is illuminated with a sheet of light created by reflecting an argon-ion laser beam from a hexagonal rotating mirror. The thickness of the resulting light sheet is 1 mm. The scattered light intensity is proportional to the local dye concentration. A monochrome video camera and standard VHS video equipment are then used to record the data, which is digitized to 8-bit precision. A background image is subtracted, but no smoothing is necessary. We find the isoconcentration levels using the algorithm described in Sec. II C.

F. Statistical characterization of isosurfaces

We compute fractal scaling functions and curvature distributions to describe the isosurfaces of temperature and concentration quantitatively, as a function of R and in different planes. To test for fractal scaling, we calculate the pointwise correlation function, defined as the average number of points $C(\epsilon)$ on the isocontour within a circle of radius ϵ centered at a given point on the contour. (It is necessary to introduce corrections to avoid bias at large ϵ from points near the edge of the image which have few neighbors, and to avoid bias at small ϵ arising from the lattice discreteness.) If the set displays fractal scaling, this function should be a power law of the form $C(\epsilon) \sim \epsilon^D$. To test for scaling we compute and display the slope $D(\epsilon) = \partial \log C(\epsilon)/\partial \log \epsilon$. We also apply a standard box counting algorithm to the data. The results are comparable, although the statistics are worse for box counting.

The curvature at a point (x,y) on the isocontour is found using the algorithm

$$\kappa = \frac{x''y' - x'y''}{(x'^2 + y'^2)^{3/2}}, \quad (3)$$

where the derivatives with respect to path length are found by locally fitting both the x and y values to second-order polynomials in the path length over segments of length n, where n is between 9 and 15 points. The curvature is calculated at each point on the isocontour [excluding points with fewer than $(n-1)/2$ neighbors on each side]. It is
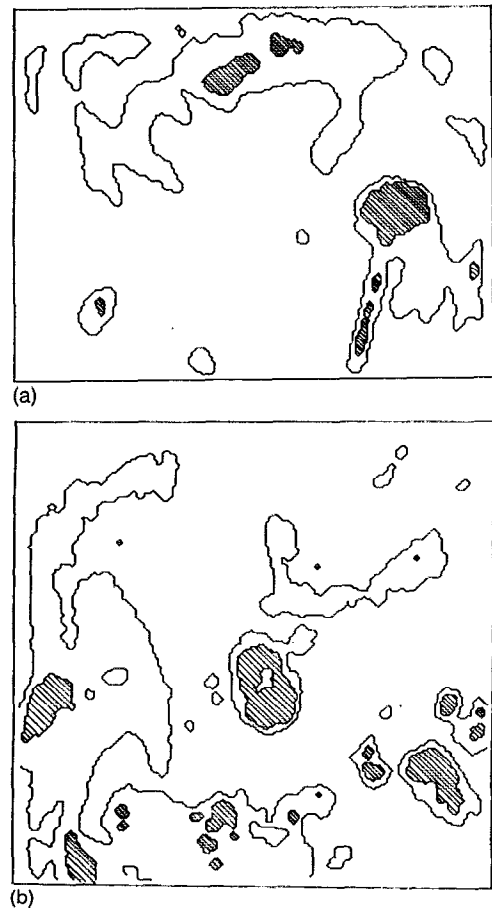

(a)

(b)

FIG. 4. Isotherms in the interior of the turbulent flow. The full vertical temperature difference is 14.4 °C, and $R = 3.4 \times 10^7$. The solid line is the mean isotherm, and the shaded regions are at least 0.2 °C above the mean. (a) Vertical plane through the center of the cell; (b) horizontal plane at the midheight of the cell. Though (a) and (b) are taken at different times, the vertical and horizontal sections of the mean isotherm are qualitatively similar.

then straightforward to compute the probability distribution of curvatures using a large number of equivalent images to obtain good statistics. The distributions are usually based on curvatures measured at 4×10^4 points or more. If the segments are too short, the low curvature regions of the distribution are distorted, while if they are too long, the high curvature regions are attenuated in the distribution. Therefore a compromise must be selected.

III. RESULTS

A. Isotherms in the interior: Qualitative observations

The isotherms in the interior of the flow at or near the mean temperature are convoluted, multiply connected surfaces. Two examples of such isotherms are shown in Figs. 4(a) and 4(b), for vertical and horizontal planes at $R = 3.4 \times 10^7$ in the 5 cm cell. The solid lines show the intersection of the isothermal surface at the mean cell temperature with the plane of illumination. (We refer to this particular isotherm henceforth as the "mean isotherm"; however, it is not an average in time or in space.) Shaded
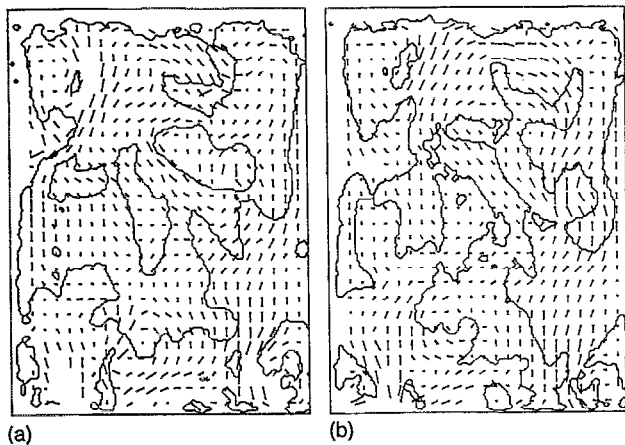
(a)   (b)

FIG. 5. Mean isotherm (solid line) and the velocity field in the same plane, shown by short flags of variable length emanating from grid points in the direction of the local velocity. (a) and (b) Vertical sections through the center of the tall cell at $R = 1.5 \times 10^8$, at times separated by 2.13 sec. The bottom (hot) boundary layer is obscured.

FIG. 6. Probability that the local temperature is higher than the mean, $P_>$, as a function of height z/d measured from the midplane at $R = 1.5 \times 10^8$. The measurement is consistent with the asymmetry of probability distribution functions of local temperature fluctuations near the boundaries.

regions correspond to areas that are least 0.2° *above* the mean temperature. In (a) (vertical plane) a large-scale flow circulates counterclockwise. A thermal plume is being emitted from the lower boundary. However, the structure of the mean isotherm is *not* determined primarily by plumes, and plumes do not always cross the mean temperature. The mean isotherm reflects in part the *oldest* structures in the interior that are not yet homogenized by the mixing and diffusion process. Though convoluted, the mean isotherms do not appear to have a great deal of structure on the smallest resolvable scales: they are relatively smooth. Another interesting qualitative feature is the fact that the area *above* the midplane is dominated by fluid *above* the mean temperature, and fluid in the lower half is primarily below the mean temperature. This feature is also evident in statistical averages (see below).

The horizontal sections are qualitatively similar to the vertical ones: the anisotropy of the flow is not very evident in the shapes of the mean isotherm. The example shown in Fig. 4(b) was taken at the midheight of the cell. The cap of a hot plume (shaded) may be seen passing through the center of the plane of observation. The area bounded by the mean isotherm fluctuates, but is on average 50% of the cell area. The shaded region, on the other hand, is bounded by an isotherm that is warmer than the mean by 4% of $\Delta T/2$. Its much smaller area is related to the nearly isothermal character of the central region of the flow.

An example of the mean isotherm structure in a vertical plane is shown in Fig. 5 at higher R with the two-dimensional velocity field superimposed. Here, the isotherms have somewhat more structure than in Fig. 4. The velocity field is shown by small flags of variable length emanating from grid points in the direction of the local velocity. It is evident that the velocity field has considerable structure on scales roughly one-fourth of the height of the cell. The Reynolds number of this flow, based on the rms velocity and this length scale, is ~100. (It would be
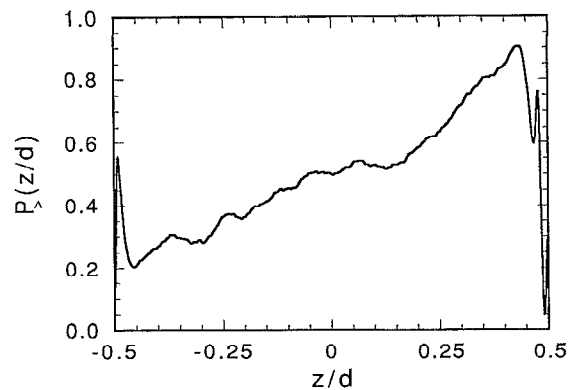
~400 based on the full cell height.) The large-scale velocity field shears the boundary layers and increases the heat extracted from them, as shown in Ref. 16. This process may be clearly seen in Fig. 5: In (a) a cold plume is being sheared off the upper boundary by the horizontal component of the velocity field. After several seconds, this structure has detached from the boundary layer and is connected with other cold structures in the center of the cell [Fig. 5(b)]. It is interesting to note that warm regions do not always rise (and vice versa); the correlation between buoyancy and velocity is quite imperfect. An example of this phenomenon may be seen at the lower right-hand corner of (a), where the cap of a *hot* plume attached to the wall is moving *downward* in the local velocity field.

The tendency of the upper half of the cell to be usually *above* the mean temperature is also evident in Fig. 5. To obtain a quantitative measure of this effect, we determine the fraction of the time (i.e., the probability $P_>$) that the local temperature is higher than the mean temperature, as a function of height. The result, again at $R = 1.5 \times 10^8$, is shown in Fig. 6. (These results reflect a temporal average over 2400 pictures, taken at 2 Hz, and a spatial average within a strip 30 pixels wide. This curve could also be obtained in principle from local temperature measurements by measuring the probability distribution function integrated from the mean temperature to the maximum temperature at each height.) We note that $P_>$ reaches 0.9 just below the *cool* boundary layer. This measurement is consistent with the fact that the local temperature probability distribution becomes quite asymmetric near the boundary layers.[3,14,16]

B. Boundary-layer dynamics

The complicated dynamics of the boundary layer can be visualized using the chiral nematic particles, supplemented by PIV. An example is shown in Fig. 7, which is a series of gray scale images of a vertical slice through the lower (hot) thermal boundary. Hot fluid appears dark here, the images are spaced 1.5 sec apart, and the bar at the
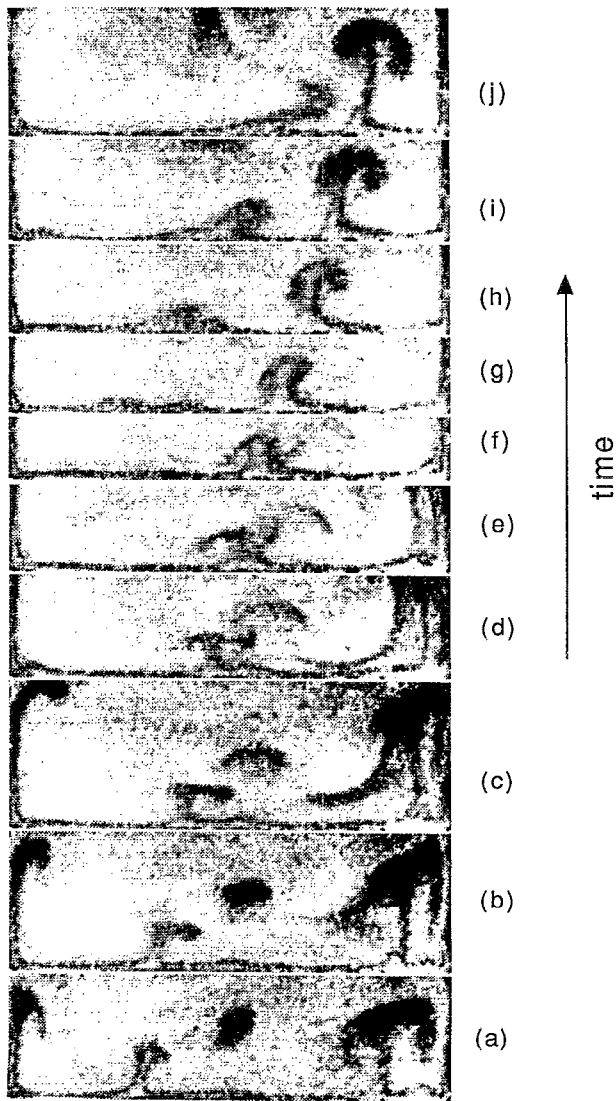
FIG. 7. Waves and eruptions of the lower thermal boundary layer at $R = 1.0 \times 10^8$. Images of the region near the boundary layer are spaced 1.5 sec apart. The hot fluid appears dark, and the bar at the lower left is 5 mm long.

FIG. 8. Warm boundary-layer height as a function of one horizontal coordinate (within a thin vertical plane) and time at $R = 1.0 \times 10^8$. The darkest regions correspond to the largest thickness, approximately 15 mm.

lower left is 5 mm long. The classical boundary-layer thickness, defined by the relationship

$$\lambda = \left(\frac{R_c \kappa \nu}{g \alpha \Delta} \right)^{1/3},$$ (4)

is 2.3 mm. The complexity of the evolution of the plumes is clearly evident in this sequence. For example, note the large plume evident in the *final* panel and follow it back in time. It is born from the interaction of several smaller structures in panels (d) and (e).

The boundary layers are not quiescent in the absence of plumes, but rather support waves and interact strongly with the velocity field. Examples of wavelike undulations of the boundary layer may be observed beginning in Fig. 7(g): they grow, propagate to the right, and are then distorted and folded by the velocity field. The actual thickness
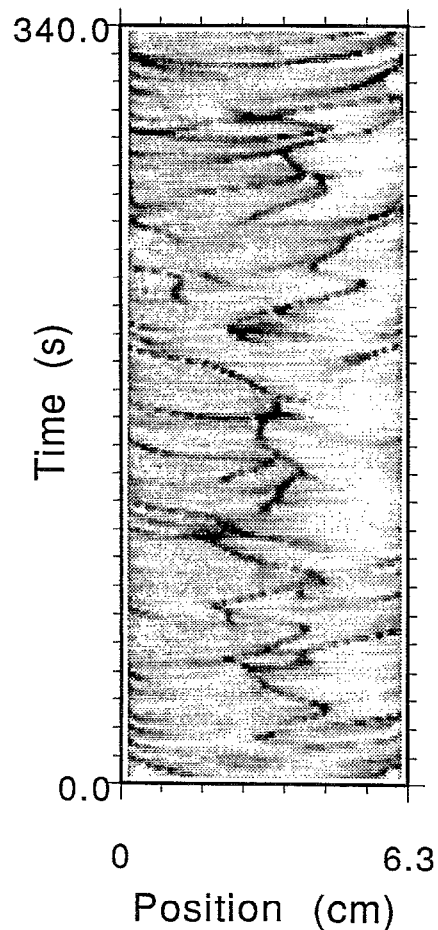
of the boundary layer varies from a small fraction of the classical boundary-layer thickness λ, to several times that value.

In order to measure the space and time dependence of the boundary-layer thickness, we define it by the height at which a vertical line (drawn vertically from the bottom of the cell) first passes through a selected threshold temperature equal to $T_m + 0.1 \Delta T$, where T_m is the mean cell temperature. A measurement of λ for the warm thermal boundary layer as a function of one horizontal coordinate and time is presented in Fig. 8. Intensity is used to label the local boundary-layer thickness, with large values shown dark. (Black corresponds approximately to 15 mm.) The large undulations and plumes, which appear as dark streaks, tend to originate near the center of the cell, and propagate toward one of the side walls. The direction frequently reverses; this implies that the large-scale flows are fluctuating and do not have a fixed sense of circulation as in some previous experiments.[6,11] Although one or more plumes are usually present, the fraction of the total area of the boundary layer occupied by the plumes is, on average, very small.
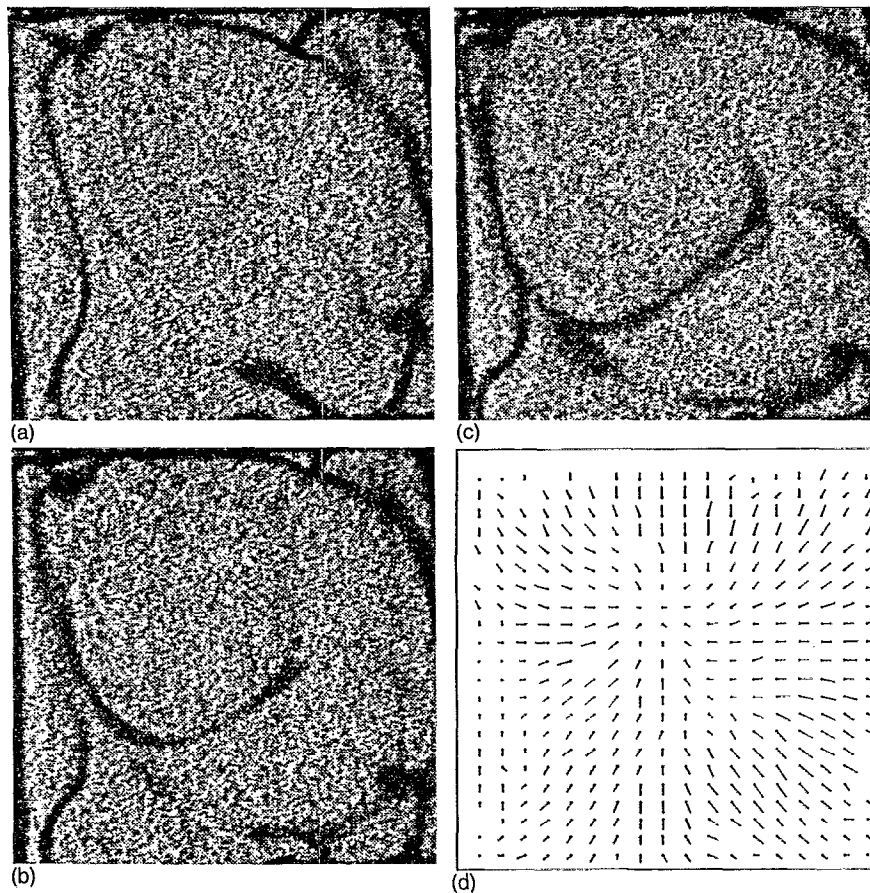
FIG. 9. (a)–(c) Undulations of the upper thermal boundary layer protruding through a horizontal plane 5 mm below the upper plate, at $R = 1.5 \times 10^8$. Cool regions are dark, and the images are spaced 1.5 sec apart. (d) Horizontal velocity field corresponding to (a).

The undulations of the boundary layer, when viewed in a *horizontal* plane, have the topology of curved lines.[4] This aspect of the geometry is illustrated in Figs. 9(a)–9(c), which consist of gray scale images from a horizontal plane located slightly (5 mm) below the upper cell boundary, and spaced 1.5 sec apart in time. The mean cell temperature is set to T_{ms}. The dark lines in these images are large amplitude undulations of the cold boundary layer piercing the plane of illumination. The nucleation of one of these lines, and its subsequent propagation, is observed near the center of panels (b) and (c). Figure 9(d) is the horizontal velocity field corresponding to (a). The velocity vectors appear to emanate from a "source" within the layer; this implies that a plume is approaching the boundary layer locally from below and spreading within the plane. The newly formed undulations often originate in regions where a large horizontal velocity *gradient* (for example, due to the impact of a plume) distorts the boundary layer. The *shape* of the evolving undulations is then determined by advection in the horizontal velocity field and buoyant forces.

C. Isotherm statistics

Since the isothermal surfaces fluctuate, it is desirable to characterize them statistically. One of the theoretical ideas that motivated this study was the suggestion[17,18] that iso-

scalar surfaces are wrinkled and possibly fractal above a length scale $\lambda^*(R)$. In order to test this concept we compute the "pointwise correlation function" $C(\epsilon)$ defined in Sec. II F. Figure 10(a) shows the behavior of $C(\epsilon/d)$ on a log–log plot, averaged over many images, and Fig. 10(b) shows the slope $D(\epsilon/d)$ as a function of ϵ/d. (Distances are normalized by the cell depth d.) The different symbols correspond to measurements in different planes.

For fractal scaling, one would expect the slope to be constant over a range of length scales, with a lower cutoff at a scale λ^*. Our observations extend down to the scale of the boundary layer, roughly 2 mm, or $\epsilon/d = 0.02$. We do not observe a well-defined scaling range. The slope varies almost continuously from about 1.2 to 1.8 over the accessible range of scales (roughly a factor of 20). The computations are quite robust; similar results are found using a box counting algorithm. The relatively smooth nonfractal character of the isotherms may well reflect the modest Rayleigh number of these experiments. We varied R over the range $10^7 < R < 3 \times 10^8$ with approximately the same results. There was not much point in going lower, and higher values are not readily available with the present apparatus and measurement techniques.

Note that no discernible dependence on orientation or height is found for the slopes in Fig. 10(b). This fact strengthens our previous qualitative observation that the
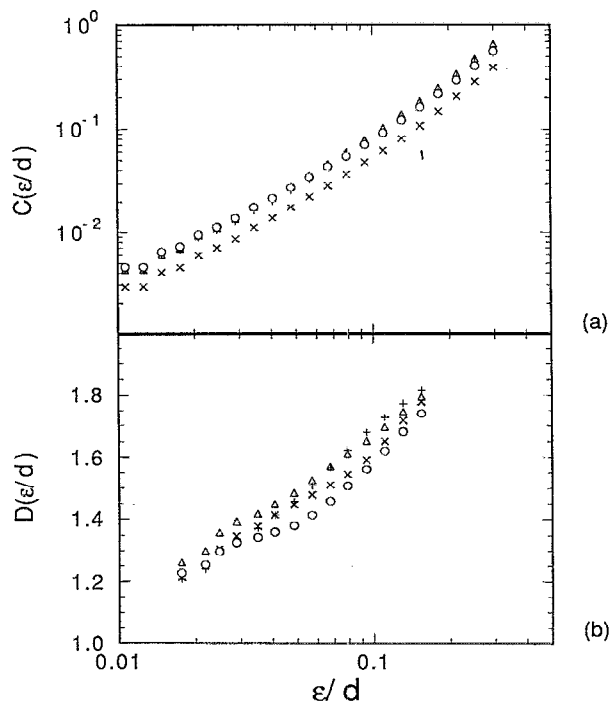
FIG. 10. (a) Pointwise correlation function $C(\epsilon/d)$ of the isotherms as a function of ϵ/d, plotted logarithmically, and (b) the local slope $D(\epsilon/d)$. Here $R=1.5\times10^8$, and results are averaged over isotherms at 24 different times. Vertical plane ($\times$); horizontal planes: midplane $z/d=0.0$ ($+$), $z/d=0.25$ ($\triangle$), $z/d=0.42$ ($\bigcirc$). The isotherms are not self-similar, but the statistics are nearly independent of location and orientation.

FIG. 11. Probability distribution function $P_T(\kappa d)$ of the curvature of the isotherms at the mean temperature, for $R=1.5\times10^8$. (a) Linear scales; (b) semilog plot. The solid line is a fit to a stretched exponential (see text). Symbols are as in Fig. 10.

geometrical character of the mean isotherms is similar for vertical and horizontal cross sections, despite the anisotropy of the *velocity* field. (However, *other* isotherms far from the mean temperature are presumably anisotropic.)

Since the isotherms are relatively smooth and are not self-similar, we characterize them alternately by computing their curvature distributions $P_T(\kappa d)$ (again using the cell depth d for normalization), as explained in Sec. II F. The results are shown in Figs. 11(a) and 11(b) for the mean isotherm at $R=1.5\times10^8$; different symbols correspond to various positions and orientations of the illuminating sheet. Each distribution is averaged over isotherms found at 24 different times, and nondimensionalized by the cell height. The two graphs contain the same data but Fig. 11(b) is plotted on a logarithmic scale. We have checked that the results are robust and not strongly dependent on the algorithm used to determine the curvature. However, the thickness of the light sheet could possibly attenuate the tails.

The distributions are strongly non-Gaussian with extended tails, and all seem to collapse onto the same distribution. This again demonstrates the statistical isotropy of the mean isotherm. The solid line in Fig. 11(b) is a fit to a stretched exponential

$$P_T(\kappa d) = Ae^{b|\kappa d|^\beta}, \qquad (5)$$

where $\beta=0.51\pm0.03$. This function provides a fairly good fit, except for the fact that positive and negative curvatures (corresponding to concave and convex shapes, respec-
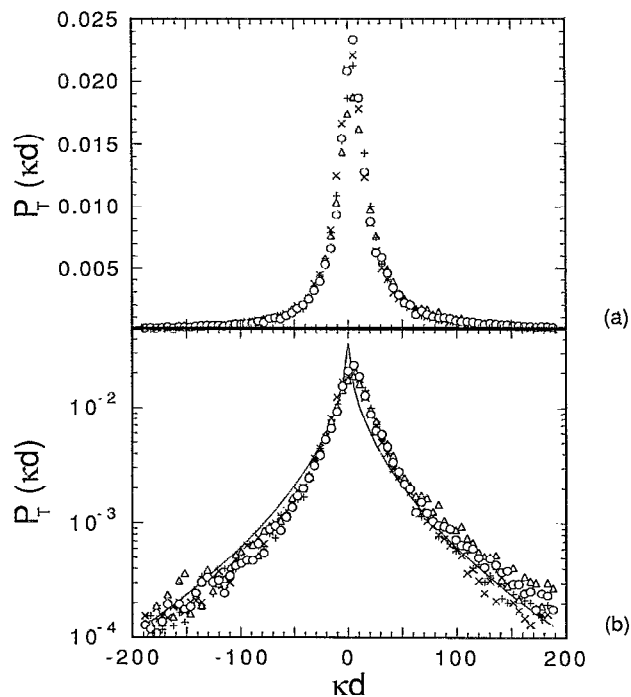
tively) are not quite equally probable. This small asymmetry could be a result of a slight temperature offset from the actual mean cell temperature. (It could also possibly be due to the violation of Boussinesq conditions.) The long tails imply that regions of high absolute curvature are considerably more likely than would be the case for a Gaussian distribution with the same variance.

Similar results are found for the isotherm corresponding to the mean cell temperature at other values of R. The standard deviation of the curvature distribution is shown as a function of R in Fig. 12. We find no clear functional
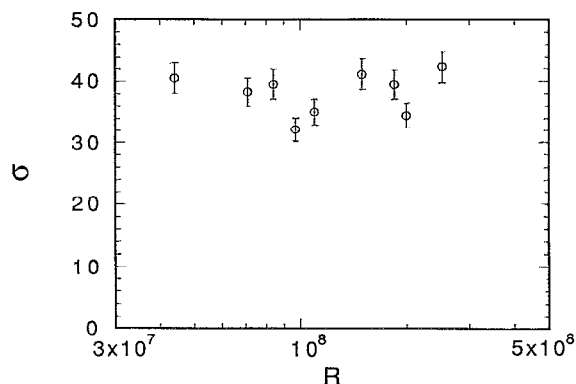

FIG. 12. Standard deviation of the curvature as a function of R. The error bars are an estimate of possible systematic errors, and are larger than the statistical errors. The variation with R is below our measurement resolution.
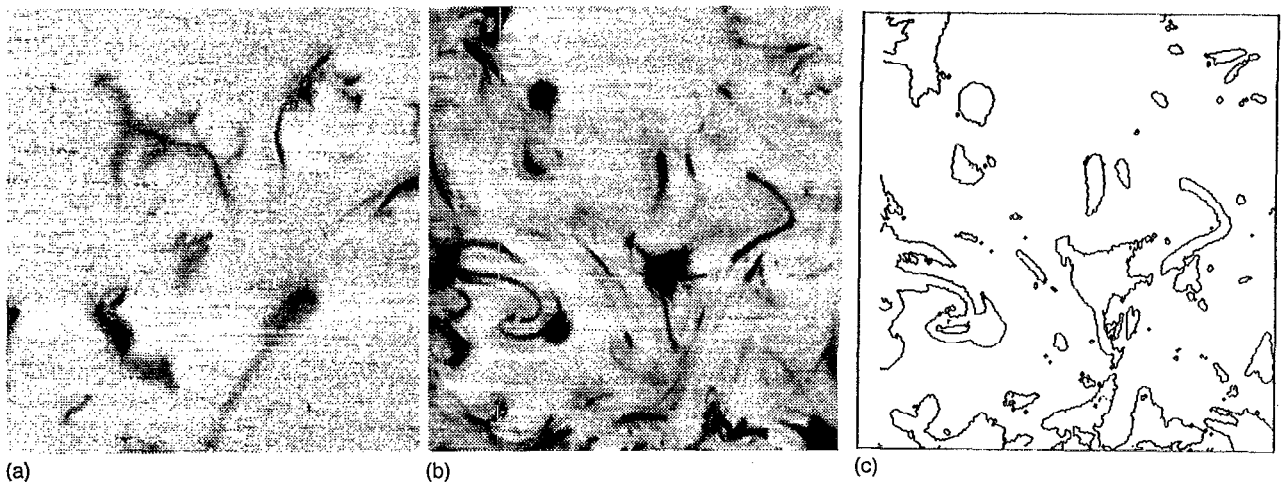
(a)　　　　　　　　　　(b)　　　　　　　　　　(c)

FIG. 13. Laser-induced fluorescence image of dye mixing (a) 30 sec and (b) 58 sec after injection, measured in the horizontal midplane at $R = 2.4 \times 10^7$. The intensity of the optical signal is proportional to the local dye concentration, but high concentrations are shown here as dark regions. (c) Isoconcentration contour derived from (b), corresponding to 25% of the maximum dye concentration.

dependence on R over the range explored. This means that the isotherms do not vary substantially in the degree to which they are convoluted over the limited range of R we have so far been able to explore. We can use the standard deviation of the curvature to determine a typical length scale $l_c/d \equiv 1/\sigma$, with the result $l_c/d \approx 0.024$ for $R \approx 10^8$. (Here $d = 9$ cm.)

D. Dye mixing

The absence of fractal scaling for the isotherms is probably a result of the relatively high value of the thermal diffusivity, as we discuss in Sec. IV. By studying the mixing of a passive quantity with a much lower diffusivity, such as a dye, it is possible to test the geometric theories in a more favorable situation. Therefore, we have also made statistical measurements of the shapes of isoconcentration contours of dye injected into the system, as a function of time. The molecular diffusivity of the dye is approximately 5×10^{-6} cm^2/sec (Ref. 34), approximately a factor of 3×10^{-3} smaller than the thermal diffusivity of water. Of course, the mixing of a localized patch of dye differs in some ways from the folding of isotherms, because the former is a transient process.

As an example, we present in Fig. 13 laser-induced fluorescence images of dye mixing in the horizontal midplane 30 and 58 sec after injection at $R = 2.4 \times 10^7$. An isoconcentration contour derived from Fig. 13(b) corresponding to 25% of the maximum concentration is shown in Fig. 13(c). Qualitatively, the dye contours quickly develop considerably more complexity than is seen in the isotherms. The mixing of the dye does not seem to be a simple stretching and folding process; even at very early times we observe thin filaments of varying sizes breaking off from the larger high concentration structures as they traverse the system. The turnover time for the large-scale circulation under the conditions of these measurements is roughly 30 sec. After just one turnover time [Fig. 13(a)]
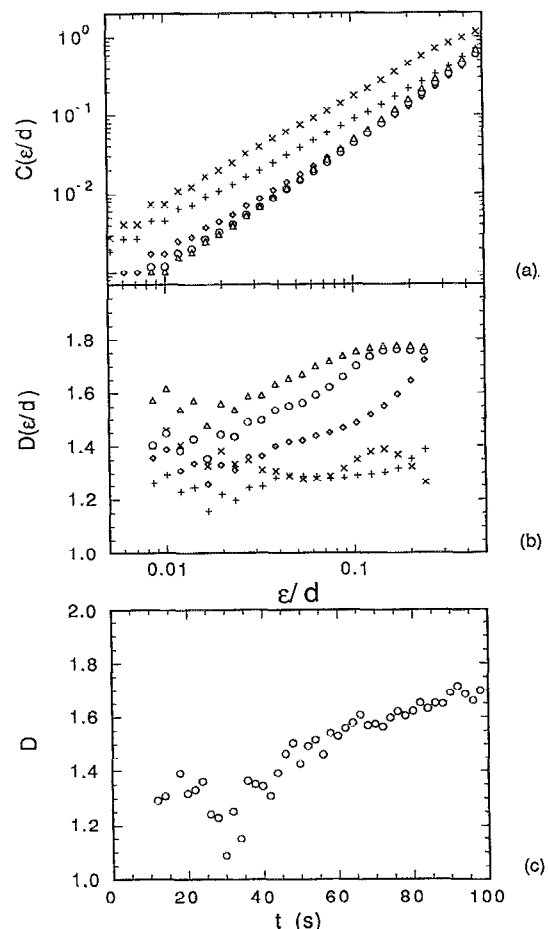

FIG. 14. (a) Logarithmic plot of the pointwise correlation function $C(\epsilon/d)$ for dye mixing at $R = 2.4 \times 10^7$, as a function of separation in units of the cell depth (5 cm). Isoconcentration surfaces at 25% of the maximum unsaturated intensity have been selected. Symbols correspond to different times (averaged over 20 sec): 0 sec ($\times$); 20 sec ($+$); 40 sec ($\Diamond$); 60 sec ($\bigcirc$); 80 sec ($\triangle$). (b) The slope $D(\epsilon/d)$ as a function of ϵ/d, for various times. (c) The slope D (averaged over ϵ) as a function of time, showing a gradual increase.
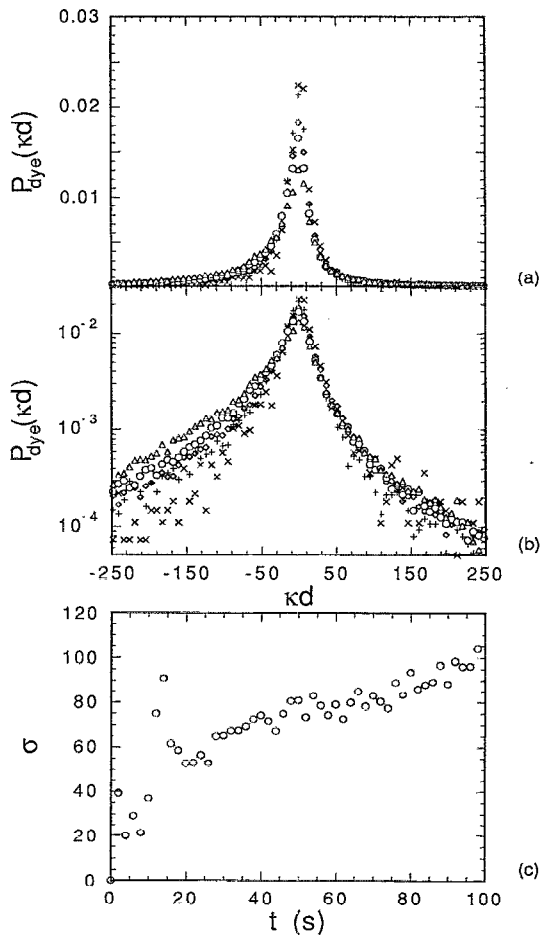
FIG. 15. (a) and (b) Curvature distributions $P_{dye}(\kappa d)$ for dye isoconcentration contours at 25% of the maximum concentration. $R=2.4\times10^7$ (5 cm cell), and the symbols are as in Fig. 14(a). (c) Standard deviation of the curvature distribution as a function of time.
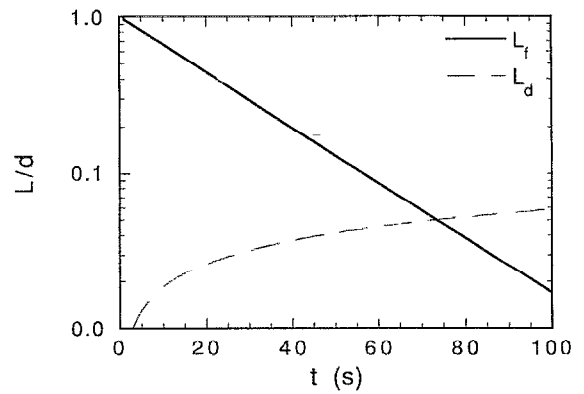

FIG. 16. Competing lengths in a model of the folding of isotherms by large-scale eddies, as a function of time: $L_f(t)$ is the decreasing length scale due to folding, with a folding time equal to the circulation time of a typical eddy at $R=1.5\times10^8$; $L_d(t)$ is the increasing length scale due to diffusion. The two cross at $t\approx75$ sec, at a length $l_f/d=0.05$.

the dye intersects the plane of illumination in many separate, disconnected areas. After two turnover times [Fig. 13(b)], both large- and small-scale structures are visible. The isoconcentration contours, one of which is shown in Fig. 13(c), also reveal structures on many scales.

In order to characterize the dye mixing process quantitatively, we have calculated the pointwise correlation function $C(\epsilon)$ of the isoconcentration contour corresponding to 25% of the maximum concentration. This computation is then repeated at 2 sec intervals during the mixing process (2–3 min total), and the results for $C(\epsilon)$ are averaged over 20 sec segments to obtain better statistics. The result is displayed in Fig. 14(a) for various times, on a log–log plot. In Fig. 14(b) we display the local slope $D(\epsilon/d)$ of the correlation function as a function of ϵ/d for the same times. At the latest time the variation of the slope with ϵ/d is substantially less than is the case for the isotherms [Fig. 10(b)]. For example, the slope is in the range 1.6 to 1.8 at the latest time shown in Fig. 4(b). Therefore it would not be unreasonable to say that there appears to be a limited range of approximate fractal scaling for the dye

contours. The approximate scaling extends down to the scale set by the light sheet ($\epsilon/d=0.02$).

The time dependence of the complexity of the dye contours is illustrated by the evolution of the slope of the correlation function (averaged over ϵ). This quantity is shown as a function of time in Fig. 14(c). The average slope D increases gradually with time as the contours become more convoluted. At long times (not shown), the fluid is well mixed, and the selected isoconcentration surface disappears. Similar results are found for various concentration levels above the final mean concentration.

The distribution of curvature $P_{dye}(\kappa d)$ for these dye isoconcentration contours is shown in Figs. 15(a) and 15(b), at different times. We note that it is asymmetric; this reflects the fact that the isoconcentration contours bound ever-shrinking islands of high dye concentration, so convex regions (with negative curvature for our conventions) are more probable than concave regions (with positive curvature). This behavior may be contrasted with that of the mean isotherm curvature distribution, which is nearly symmetric. However, each side of the distribution can be fitted by a stretched exponential, and again the exponent $\beta=0.5\pm0.05$. The standard deviation σ of the curvature, shown in Fig. 15(c), increases gradually with time. (The early measurements have a large uncertainty, so the fluctuations for $t<20$ sec are not significant.) At long times the islands become very small, and the measurement loses significance after about 100 sec. As in the case of the isotherms, we use the reciprocal of σ to determine a curvature length scale; it *decreases* with time from $l_c/d\approx0.05$ shortly after injection to $l_c/d\approx0.01$ at late times. (For the dye measurements, $d=5$ cm.)

IV. CHARACTERISTIC SCALES: A COMPARISON

This work was stimulated in part by the suggestion[17,18] that for sufficiently high R, isotherms might exhibit scaling above a cutoff length scale λ^* given by Eq. (2). The salient facts are that the isotherms at the mean temperature do not

show fractal scaling in our experiments, while the isoconcentration surfaces in transient mixing do appear to show an appreciable scaling range. Furthermore, the curvature scale l_c/d is a factor of 2–3 smaller for the dye mixing.

To understand these observations, it may be useful to note that our measurements single out the isotherm at the mean temperature. This choice was motivated by two factors: the symmetry of the system with respect to the mean temperature; and the desirability of avoiding regions near the boundaries. This latter goal can only be accommodated by selecting temperatures near the mean temperature isotherm, since temperatures deviating strongly from the mean are found only rarely in the interior. The mean isotherm is primarily related to the oldest thermal structures in the system, those which have broken off from the boundary layer in the past and have been convected around the interior by the large-scale flow. The velocity fluctuations which tend to deform this isotherm are primarily the *large eddies* in the flow, and not the smaller scales that are more prevalent near the boundaries and which are assumed in Refs. 17 and 18.

Provisionally adopting this viewpoint, we imagine a simple model in which the geometry of the isotherm at the mean temperature is governed by a competition between simple folding by the large-scale eddies, and diffusion. We consider a very simple model in which a thermal structure bounded by an isotherm is *folded* once every time step. Such a folding process, while it does produce complexity, need not lead to well-defined scaling behavior. The characteristic length scale due to the folding decays with time roughly according to the expression $L_f(t) = d \times \exp(-t/\tau_f)$, where d is the initial size of the structure, roughly the height of the cell, and τ_f is the folding time. Diffusion, on the other hand, smoothes the isotherm over a distance given roughly by $L_d(t) = \sqrt{2\kappa t}$. We assume that the *oldest* structures that are detectable are those for which $L_d \approx L_f$. We define this crossover to be the *folding scale* l_f.

In Fig. 16, we show L_f and L_d as a function of time using a folding time $\tau_f \approx 25$ sec that is typical for $R = 1.5 \times 10^8$; this is roughly the circulation time of a typical large eddy as seen in Fig. 5. The diffusion and folding lengths intersect near $t = 75$ sec, and the resulting folding scale is $l_f/d = 0.05$, or 4 mm. The estimate is not very sensitive to the folding time; reducing τ_f by a factor of 2 reduces this length scale by only 25%. The length scale for the oldest observable structures predicted by this simple folding model is in fact comparable to the typical length scale of the mean isotherms, $l_c/d \approx 0.024$, as determined by the inverse of the standard deviation of the curvature distribution.

We now turn to the behavior of the isoconcentration contours for dye dispersal, for which rough scaling behavior is in fact observed over a decade or so. It is important to recognize that the transient process of dye dispersal is significantly different from the steady-state behavior of the mean isotherms, so application of the folding model given above is questionable. However, the model does in fact give a reasonable estimate. The folding scale l_f/d is easily found to be approximately 0.007 for the conditions of the experiments in Sec. III D, a value that compares rather well to the measured curvature scale l_c/d at late times. The isoconcentration contours evolve to somewhat smaller scales than the isotherms, even at a *lower* Rayleigh number.

The application of the ideas of Refs. 17 and 18 to our experiments is probably marginal given the fact that the Rayleigh number R is only within the "hard turbulence" regime by about 1 decade, and the Reynolds number based on the full cell height is somewhat less than 10^3. The difficulties with applying that approach to our experiments is illustrated by estimating the value it predicts for the ratio of the two cutoff scales:

$$\frac{\lambda^*_{dye}}{\lambda^*_{heat}} = \left(\frac{\kappa_{dye}}{\kappa}\right)^{1/(1+\zeta)} \approx (10^{-3})^{1/(1+\zeta)}. \qquad (6)$$

For $\zeta = 1/3$, this ratio is about 5×10^{-3}, a much more dramatic effect of changing the diffusivity than is actually observed. However, the thickness of our light sheet is sufficiently large that we would be unable to detect fluctuations on scales much smaller than the observed l_c.

V. SUMMARY AND CONCLUSION

We have shown that liquid crystal imaging can be used to make quantitative measurements of the temperature field in turbulent Rayleigh–Bénard convection. The experiments focused especially on the geometry of the isotherm at the mean temperature of the fluid (the "mean isotherm") in various vertical and horizontal planes away from the boundaries of the cell. This isotherm is important because it reflects the oldest thermal structures in the flow, those that have had the longest time to develop spatial complexity. Though the mean isotherm is hard to study because of the nearly isothermal conditions in the bulk of the flow, we were able to study its geometry with resolution of about 1 mm with judicious use of image processing techniques.

Combining the thermal measurements with particle image velocimetry, we illustrated some of the complicated interactions involving the velocity field and undulations of the thermal boundary layer. These spatially extended undulations or unstable waves appear to be frequently nucleated on the boundary layer in regions of high horizontal velocity *gradient* (Fig. 9). This result seems reasonable, since high horizontal gradients lead to compression or dilatation of the boundary layer. The undulations give rise to thermal plumes that are convected erratically through the interior of the flow by the large-scale eddies. The thermal measurements also show (Fig. 6) that the temperature is more frequently *above* the mean temperature in the upper half of the cell (near the cool surface) and more frequently *below* the mean in the lower half (near the warm surface).

We find that the mean isotherm is a convoluted multiply connected surface, but that it is not fractal for R near 10^8, a result that might be expected given the very modest Reynolds number. The most useful method of characterizing the isotherm geometry statistically seems to be the probability distribution $P_T(\kappa d)$ of the local curvature (e.g., Fig. 11). This function is strongly non-Gaussian, and

is approximately described as a stretched exponential. Unfortunately, due to the light sheet thickness, the measurement resolution is not sufficiently small to ensure that the tails of the distribution are accurately measured.

As far as we are aware, a theoretical prediction for the shape of the isotherm curvature distribution is not available. However, the distribution of temperature gradients is expected[35] to be of stretched exponential form with an exponent of 0.5, and *temporal* temperature differences have been shown to have this form.[36,37] It is interesting to speculate on the possible connections between our observations of curvature distributions and this work on temperature gradient and differences.

The standard deviation of the curvature yields a length scale l_c that is typically a few millimeters; its dependence on R is not detectable over the limited range of our experiments. The curvature scale can be estimated approximately with the aid of a simple folding model, by considering the balance between an exponentially decreasing folding scale and a diffusion scale growing as $t^{1/2}$ (Fig. 16).

By measuring $P_T(\kappa d)$ as a function of the position and orientation of the measurement plane, we determined that the mean isotherm is statistically isotropic and independent of height (to within the experimental precision). These facts imply that the geometrical structure of the mean isotherm at small scales is not strongly influenced by the buoyancy that drives the large scales. The observation of isotropy within the central region of the cell is consistent with recent work by Chillá *et al.*[38] Using a laser beam sweeping technique, they measured the temperature $\bar{T}(x,z,t)$, averaged along one of the horizontal directions (y) in thermal turbulence. They found that power spectra of the temperature field for wave numbers k_x and k_z were essentially identical. One might wonder whether the significantly non-Boussinesq conditions of our experiments could lead to a substantial anisotropy; however, this appears not to be the case in the central region of the flow, probably because the conditions there are nearly isothermal. This trend has also been noted in numerical simulations by Frölich *et al.*[39]

In contrast to the behavior of the isotherms, the isoconcentration surfaces of a passive scalar, a fluorescent dye injected into the flow, do seem to have an appreciable scaling range. However, the mixing is a transient process, so the apparent dimension depends on time and on the selected concentration level. The curvature distribution for isoconcentration contours is asymmetric, and its standard deviation σ grows steadily during the mixing process. (We could not tell whether σ eventually saturates, because the fluorescence intensity fluctuations become too weak at long times.) The curvature scale l_c/d for dye mixing is roughly a factor of 2–3 below that for the isotherms. We were unable to determine conclusively whether all of the scales present in the isoconcentration contours were fully resolved, due to the finite thickness of the light sheet.

It would be of interest to investigate the geometry of isotherms at much higher Rayleigh numbers. However, the liquid crystal imaging method is delicate, so this probably cannot be accomplished simply by scaling up the present experiment to a much larger volume of fluid.

ACKNOWLEDGMENTS

[1]M. C. Cross and P. C. Hohenberg, "Pattern formation outside of equilibrium," Rev. Mod. Phys. (in press).

[2]E. M. Sparrow, R. B. Husar, and R. J. Goldstein, "Observations and other characteristics of thermals," J. Fluid Mech. **41**, 793 (1970).

[3]H. Tanaka and H. Miyata, "Turbulent natural convection in a horizontal water layer heated from below," Int. J. Heat Mass Transfer **23**, 1273 (1980).

[4]T. Asaeda and K. Watanabe, "The mechanism of heat transport in thermal convection at high Rayleigh numbers," Phys. Fluids A **1**, 861 (1989).

[5]S. Gross, G. Zocchi, and A. Libchaber, "Ondes et plumes de couche limite thermique," C. R. Acad. Sci. Paris **307**, 447 (1988).

[6]G. Zocchi, E. Moses, and A. Libchaber, "Coherent structures in turbulent convection, and experimental study," Physica A **166**, 387 (1990).

[7]M. J. Shelley and M. Vinson, "Coherent structures on a boundary layer in Rayleigh–Bénard turbulence," Nonlinearity **5**, 323 (1992).

[8]F. Heslot, B. Castaing, and A. Libchaber, "Transitions to turbulence in helium gas," Phys. Rev. A **36**, 5870 (1987).

[9]M. Sano, X.-Z. Wu, and A. Libchaber, "Turbulence in helium-gas free convection," Phys. Rev. A **40**, 6421 (1989).

[10]X.-Z. Wu and A. Libchaber, "Scaling relations in thermal turbulence: The aspect-ratio dependence," Phys. Rev. A **45**, 842 (1992).

[11]R. Krishnamurti and L. N. Howard, "Large-scale flow generation in turbulent convection," Proc. Natl. Acad. Sci. USA **78**, 1981 (1981).

[12]T. H. Solomon and J. P. Gollub, "Sheared boundary layers in turbulent Rayleigh–Bénard convection," Phys. Rev. Lett. **64**, 2382 (1990).

[13]S. L. Christie and J. A. Domaradzki, "Numerical evidence for nonuniversality of the soft/hard classification for thermal convection," Phys. Fluids A **5**, 412 (1993).

[14]B. Castaing, G. Gunaratne, F. Heslot, L. Kadanoff, A. Libchaber, S. Thomae, X.-Z. Wu, S. Zaleski, and G. Zanetti, "Scaling of hard thermal turbulence in Rayleigh–Bénard convection," J. Fluid Mech. **204**, 1 (1989).

[15]B. I. Shraiman and E. D. Siggia, "Heat transport in high-Rayleigh-number convection," Phys. Rev. A **42**, 3650 (1990).

[16]T. H. Solomon and J. P. Gollub, "Thermal boundary layers and heat flux in turbulent convection: The role of recirculating flows," Phys. Rev. A **43**, 6683 (1991).

[17]I. Procaccia, E. S. C. Ching, P. Constantin, L. P. Kadanoff, A. Libchaber, and X.-Z. Wu, "Transitions in convective turbulence: The role of thermal plumes," Phys. Rev. A **44**, 8091 (1991).

[18]P. Constantin, I. Procaccia, and K. R. Sreenivasan, "Fractal geometry of isoscalar surfaces in turbulence: Theory and experiments," Phys. Rev. Lett. **67**, 1739 (1991).

[19]H. Tennekes and J. L. Lumley, *A First Course in Turbulence* (MIT Press, Cambridge, MA, 1972).

[20]R. H. Kraichnan, Phys. Rev. Lett. **67**, 3634 (1991).

[21]R. R. Prasad and K. R. Sreenivasan, "The measurement and interpretation of fractal dimensions of the scalar interface in turbulent flows," Phys. Fluids A **2**, 792 (1990).

[22]P. L. Miller and P. E. Dimotakis, "Stochastic geometric properties of scalar interfaces in turbulent jets," Phys. Fluids A **3**, 168 (1991).

[23]K. R. Sreenivasan and A. Juneja, "Fractal dimensions of time series in turbulent flows" (to be published).

[24]R. Ramshankar and J. P. Gollub, "Transport by capillary waves. Part II: Scalar dispersion and structure of the concentration field," Phys. Fluids A **3**, 1344 (1991).

[25]R. Ramshankar and J. P. Gollub, "Transport by capillary waves. Part I: Particle trajectories," Phys. Fluids A **2**, 1955 (1990).

660   Phys. Fluids A, Vol. 5, No. 3, March 1993

Gluckman, Willaime, and Gollub   660

[26] I. Procaccia and P. Constantin, "The fractal geometry of the level sets of a contaminant dispersed by chaotic surface waves" (to be published).

[27] E. Ott and T. M. Antonsen Jr., "Chaotic fluid convection and the fractal nature of passive scalar gradients," Phys. Rev. Lett. **61**, 2839 (1988).

[28] T. M. Antonsen Jr. and E. Ott, "Multifractal power spectra of passive scalars convected by chaotic fluid flows," Phys. Rev. A **44**, 851 (1991).

[29] N. Kasagi, R. J. Moffat, and M. Hirata, in *Handbook of Flow Visualization*, edited by W.-J. Yang (Hemisphere, New York, 1989), p. 105.

[30] D. Dabiri and M. Gharib, "Digital particle image thermometry: The method and implementation," Exp. Fluids **11**, 77 (1991).

[31] The relationship between the two color systems is shown graphically on the color wheel in the "control panel" of Macintosh II computers.

[32] R. J. Adrian, "Multi-point optical measurements of simultaneous vectors in unsteady flow—A review," Int. J. Heat Fluid Flow **7**, 127 (1986).

[33] C. E. Willert and M. Gharib, "Digital particle image velocimetry," *Exp. Fluids* **10**, 181 (1991).

[34] B. R. Ware, D. Cyr, S. Gorti, and F. Lanni, in *Measurement of Suspended Particles by Quasi-elastic Light Scattering*, edited by B. E. Dahneke (Wiley, New York, 1983), p. 255.

[35] E. D. Siggia and B. Shraiman (private communication).

[36] E. S. C. Ching, "Probability densities of turbulent temperature fluctuations," Phys. Rev. Lett. **70**, 283 (1993).

[37] E. S. C. Ching, "Probabilities for temperature differences in Rayleigh–Bénard convection," Phys. Rev. A **44**, 3622 (1991).

[38] F. Chillá, C. Innocenti, and S. Ciliberto, "Spectra of local and averaged scalar fields in turbulence" (to be published).

[39] J. Fröhlich, P. Laure, and R. Peyret, "Large departures from Boussinesq approximation in the Rayleigh–Bénard problem," Phys. Fluids A **4**, 1355 (1992).